arXiv:1507.03406v2 [quant-ph] 20 Jul 2015

Bosonic transport simulations in a large-scale programmable nanophotonic processor

Nicholas C. Harris*,[1] Gregory R. Steinbrecher*,[1] Jacob Mower,[1] Yoav Lahini,[2] Mihika Prabhu,[1] Tom Baehr-Jones,[3] Michael Hochberg,[3] Seth Lloyd,[4] and Dirk Englund[1]

[1)] *Department of Electrical Engineering and Computer Science, Massachusetts Institute of Technology, 77 Massachusetts Avenue, Cambridge, MA 02139, USA*

[2)] *Department of Physics, Massachusetts Institute of Technology, 77 Massachusetts Avenue, Cambridge, MA 02139, USA*

[3)] *Coriant Advanced Technology, 171 Madison Avenue, Suite 1100, New York, NY 10016, USA*

[4)] *Department of Mechanical Engineering, Massachusetts Institute of Technology, 77 Massachusetts Avenue, Cambridge, MA 02139, USA*

Environmental noise and disorder play a critical role in quantum particle and wave transport in complex media, including solid-state and biological systems. Recent work has predicted that coupling between noisy environments and disordered systems, in which coherent transport has been arrested due to localization effects, could actually enhance transport. Photonic integrated circuits are promising platforms for studying such effects, with a central goal being the development of large systems providing low-loss, high-fidelity control over all parameters of the transport problem. Here, we fully map out the role of static and dynamic disorder in quantum transport using a low-loss, phase-stable, nanophotonic processor consisting of a mesh of 56 generalized beamsplitters programmable on microsecond timescales. Over 85,600 transport experiments, we observe several distinct transport regimes, including environment-enhanced transport in strong, statically disordered systems. Low loss and programmability make this nanophotonic processor a promising platform for many-boson quantum simulation experiments.

Quantum walks (QWs), the coherent analogy to classical random walks, have emerged as a useful model for experimental simulations of quantum transport (QT) phenomena in physical systems. QWs have been implemented in platforms including trapped ions[1,2], ultra-cold atoms[3], bulk optics[4–8] and integrated photonics[4,9–16]. Integrated photonic implementations are particularly attractive for relatively large coherence lengths, high interferometric visibilities, integration with single-photon sources[17,18] and detectors[19], and the promise of scaling to many active and reconfigurable components. The role of static and dynamic disorder in the transport of quantum walkers has been of particular interest in the field of quantum simulation[20,21].

Control over static (time-invariant) and dynamic (time-varying) disorder enables studies of fundamentally interesting and potentially useful QT phenomena in discrete-time (DT) QWs. In systems with strong dynamic disorder, illustrated in Fig. 1(a), a quantum walker evolving over T time steps travels a distance proportional to $\sqrt{T}$; the coherent nature of the quantum walker is effectively erased, resulting in classical, diffusive transport characteristics[22,23]. In contrast, a quantum walker (or coherent wave) traversing an ordered system travels a distance proportional to T as a result of coherent interference between superposition amplitudes — a regime known as ballistic transport (see Fig. 1(b)). Perhaps most notably, a quantum walker propagating through a system with strong, static disorder becomes exponentially localized in space and time, inhibiting transport, as illustrated in Fig. 1(c). This QT phenomena is known as Anderson localization[24] and it has been observed in several systems, including optical media[9–11,25,26]. For systems in which transport has been arrested due to Anderson localization, it has recently been predicted that adding environmental noise (dynamic disorder), over a finite range of strengths, could result in enhanced transport. This effect, known as environment-assisted quantum transport (ENAQT), is believed to play a key role in the high transport efficiencies in continuous-time photosynthetic complexes[27,28]. With such a variety of QT phenomena accessible, it is of fundamental interest to develop systems capable of fully probing the disorder space — potentially revealing new QT phenomena in the single- and multi-particle regimes.

In integrated photonic systems, static and dynamic disorder have been introduced by fabricating circuits with random parameter variations or post-processing[9,11] — rendering explorations of large parameter spaces in QT simulations possible, but cumbersome. Further, single realizations of disorder are not suitable to characterize transport as they can produce a wide range of output distributions[10]; ensemble averages over many realizations are necessary to accurately reproduce output statistics. While static and dynamic disorder have been studied separately[4,9–12,22], transport in a system capable of implementing both simultaneously — a requirement for the observation of ENAQT — in all combinations and strengths, with low loss, and over a large number of realizations has not been demonstrated[29]. Developing systems capable of meeting these requirements, and the more stringent requirement of generating arbitrary single-particle unitary operations[30], has been the topic of several recent theoretical investigations[31,32].

Here, we investigate the effect of all combinations of static and dynamic disorder strengths on the transport efficiency of a single-particle undergoing a DT, symmetric QW. Over 5,600 experiments, we probe the spatiotemporal evolution of a quantum walker traversing the system under several distinct transport regimes. To determine whether ENAQT can occur in DT systems maintaining a strong static disorder component, we perform 80,000 experiments spanning

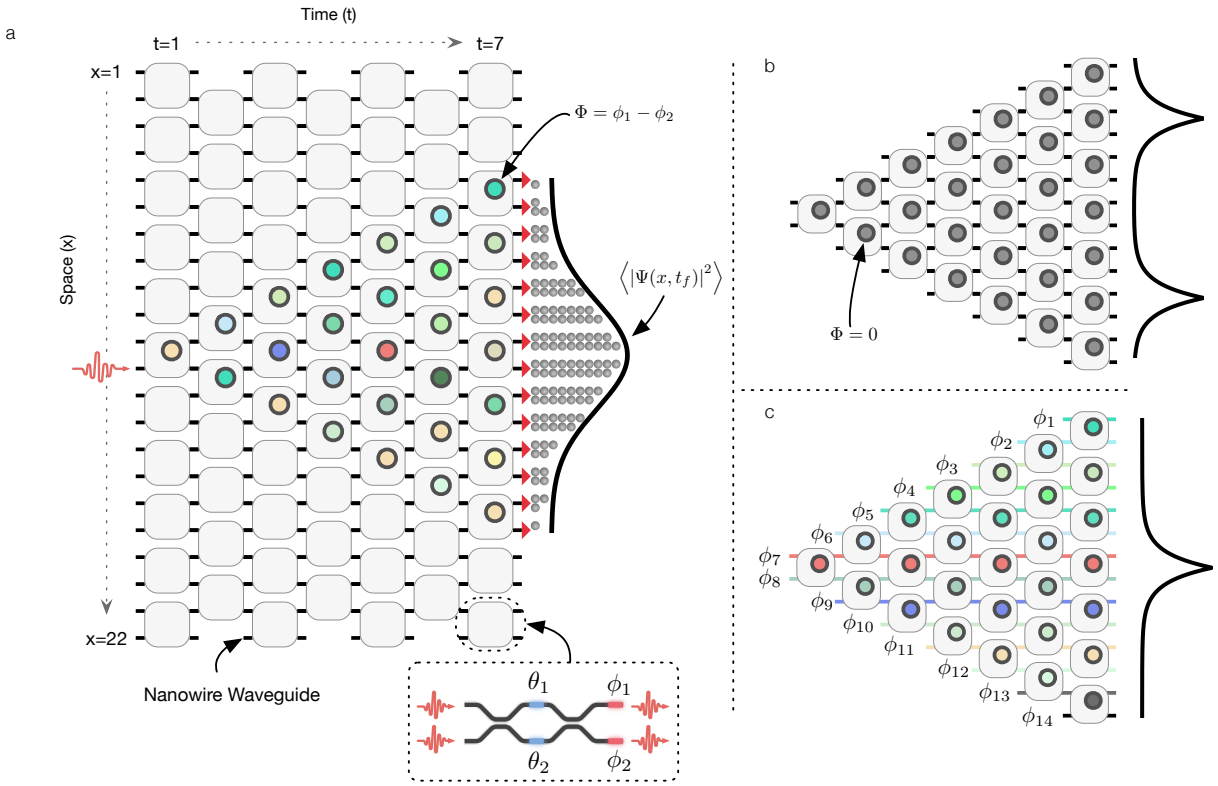

FIG. 1. **Conceptual representation of quantum transport experiments.** Schematic of programmable nanophotonic processor. Horizontal lines represent nanowire waveguides; boxes represent 4-port reconfigurable beamsplitter ((see lower inset of (a); thermal phase modulators control the splitting ratio via $\theta_{1,2}$ and the phase shift between steps via $\phi_{1,2}$)). Time is defined from left to right; space is defined from top to bottom. Colored regions represent output differential phase setting Φ. (a) Output phases are randomized, resulting in incoherent, diffusive transport shown conceptually with a Galton's board representation at the last time step. (b) Ballistic propagation configuration. The quantum walker is most likely found along the outer modes of the PNP in the absence of phase disorder. (c) Anderson localization configuration. The quantum walker is mainly confined to the central modes in the presence of strong static phase disorder (the phase setting on a given waveguide mode is constant in time and denoted by ϕ_i).

400 unique combinations of static and dynamic disorder. Our data show an enhancement in the transport efficiency of a quantum walker in systems with strong static disorder as dynamic disorder is increased.

The 85,600 experimental realizations of QWs are enabled by a large-scale, low-loss, phase-stable programmable nanophotonic processor (PNP) that provides complete control over static and dynamic disorder as well as coupling rates in QWs. Previously, photonic integrated circuits for quantum information processing have been limited to 30 individually tunable elements and 15 interferometers[33]. The PNP is composed of 213 individually tunable phase modulators and 56 interferometers spanning a chip area of 4.9 mm by 1.7 mm. This high component density is enabled by high silicon-to-silica index contrast (enabling the fabrication of waveguides with bend radii down to 2 μm[34]) and the large thermo-optic coefficient of silicon (enabling compact phase modulators[35]).

We consider random walks of a single photon (boson), which are characterized by output intensities identical to those obtained with coherent light. While single-particle statistics are easily calculated on classical computers, the Hilbert space occupied by a state of n identical photons scales exponentially with n — recent work suggests that even sampling the output distributions from linear unitary processes, including QWs, with a relatively small numbers of photons ($n > 30$ for a circuit with approximately 1000 modes) becomes intractable for classical computers[36–38]. Further, QWs augmented with feed-forward control[39–41] could be used in universal quantum computation schemes[42]. These single-particle QT simulations performed using our large-scale, low-loss, phase-stable, and high fidelity PNP mark an important step towards post-classical computing and quantum simulation applications in the multi-particle regime.

PROGRAMMABLE NANOPHOTONIC PROCESSOR

The PNP, shown in Fig. 2(a), consists of a mesh of reconfigurable beamsplitters (RBS). Each RBS is composed of two 50% directional couplers separated by two internal ($\Theta = \theta_1 - \theta_2$) and two external ($\Phi = \phi_1 - \phi_2$) thermo-optic phase shifters[35], as shown in Fig. 2(b, c). Redun-

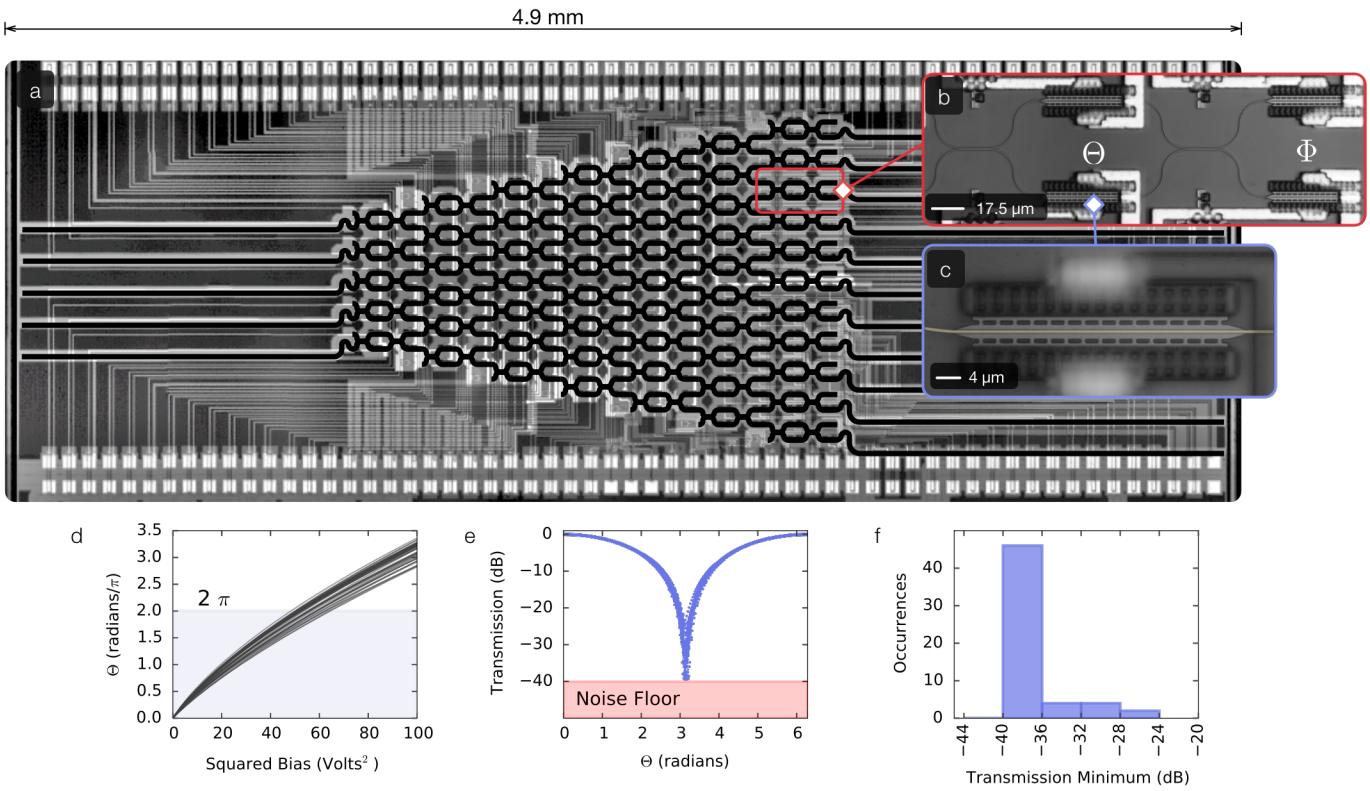

FIG. 2. **Optical micrographs of programmable nanophotonic processor.** (a) The system is 4.9 mm by 1.7 mm and is composed of 56 Mach-Zehnder interferometers, 213 phase shifters, and 112 directional couplers. Waveguides are outlined in black. (b) RBS unit cell with two directional couplers and two internal ($\theta_{1,2}$) and two external ($\phi_{1,2}$) low-loss, thermo-optic phase shifters. (c) Thermo-optic phase shifter. Heat is localized to the waveguide using narrow thermal bridges. (d) Phase versus squared bias and (e) transmission versus phase for all 56 internal phase shifters in the light cone. All elements exceed 2π radians phase shift with an average interferommetric visibility of 0.9993 $\pm$ 0.0002. (f) Histogram of transmission minima; the majority of interferometers have minima at the noise floor of our experimental setup.

dancy in internal and external phase shifters balances loss, increasing interferometric visibility for the single- and meta-interferometers that compose the PNP. The RBS applies the SU(2) rotation,

$$\hat{U}_{RBS} = \begin{bmatrix} e^{i\Phi}\sin(\Theta) & e^{i\Phi}\cos(\Theta) \\ \cos(\Theta) & -\sin(\Theta) \end{bmatrix}$$

in the spatial-mode basis. Each RBS can implement any rotation in SU(2) by using its internal and external phase shifters and the output phase shifter of the preceding RBS; for the input RBSs in the PNP, all of SU(2) can be accessed by choosing an input phase.

As shown in Fig. 2(a), the RBS lattice of the PNP is staggered such that a particle in the top port of an RBS will enter the bottom port of an RBS in the next layer. This nearest-neighbor coupling is described by

$$i\frac{\partial}{\partial t}\hat{a}_x^\dagger = C_{x,x+1}\hat{a}_{x+1}^\dagger + C_{x,x-1}\hat{a}_{x-1}^\dagger,$$

where x is the spatial coordinate shown in Fig. 1(a), $C_{x,x+1}$ ($C_{x,x-1}$) is the amplitude associated with transitioning to a higher (lower) mode at each layer, respectively, and $\hat{a}$ is the mode annihilation operator.

The thermo-optic response of all 56 internal RBS phase shifters within the single-input light cone used in this experiment is shown in Fig. 2(d); all phase shifters reach beyond 2π radians of imparted phase. Transmission curves and histogram for the RBS unit cells are shown in Figs. 2(e) and (f), with a mean visibility V of 0.9993 $\pm$ 0.0002 ($V = (I_{max} - I_{min})/(I_{max} + I_{min})$, where I_{max}, I_{min} are measured optical intensities in Watts). The sub-linearity in Fig. 2(d) is attributed to electron velocity saturation; variation in phase results from contact resistance differences across the 240 electronic probe pads on the PNP chip.

For bias levels corresponding to $\theta, \phi \in [0, 2\pi]$, thermal cross-talk between phase shifters results in a transmission change in nearby RBSs of less than -40 dB — the dynamic range of our experimental setup. The thermo-optic modulators have a 3 dB bandwidth of 130.0 $\pm$ 5.59 kHz[35], permitting up to 10^5 full PNP reconfigurations per second. The on-chip transmission loss through the PNP was measured to be less than 2.0 dB and is attributed to waveguide propagation loss[43]. The PNP was fabricated in a complimentary metal-oxide semiconductor (CMOS) - compatible, silicon photonics process (see Methods for more

detail). Waveguide edge roughness results in minor differences in path lengths between the arms of individual RBS unit cells[44]. We eliminated this problem by calibrating the PNP and programming it to implement a known unitary operation (see Supplemental Information for details on calibration).

To program all 213 phase shifters, we developed a 240-channel electronic biasing printed circuit board (PCB) capable of driving all channels from 0 to 12 volts with 183 μV discretization. To measure the PNP output mode intensities, we developed a 12-channel photodiode array PCB with approximately 40 dB of dynamic range per channel. See the Supplemental Information for experimental setup details.

EXPERIMENT

As illustrated in Fig. 1(a), we use a spatial encoding for the position (x) of the quantum walker with the axial coordinate (t) defined at each layer of RBSs. The settings for the QW program are shown in Fig. 3(a). In the first time step, we excite the bottom waveguide mode ($x = 8$) and program the first RBS as $(\Theta, \Phi) = (\pi/2, \pi/2)$ giving the output state (up to a global phase) $|\Psi\rangle \rightarrow \frac{1}{\sqrt{2}}(|t\rangle + i\,|b\rangle)$, where t (b) is the top (bottom) output mode of an RBS. We program all subsequent RBSs as Hadamard gates $(\pi/2, 0)$,

$$\hat{H} = \frac{1}{\sqrt{2}} \begin{bmatrix} 1 & 1 \\ 1 & -1 \end{bmatrix},$$

ensuring that the upward traveling terms in the superposition are $\pi/2$ out of phase with the downward traveling terms and yielding a symmetric QW.

Static and dynamic disorder are applied by randomly varying Φ while holding Θ constant. Output phases are labeled as $\Phi_{x,t}$, where '(x,t)' is a coordinate in the space-time of the QW. Static disorder is controlled by selecting phases from the uniform distribution ($\mathcal{U}[-\pi, \pi]$) over the position space of the QW $\Phi_{x,t} = 2\pi c_{tid} \cdot \mathcal{U}[-\pi, \pi]$ for each x, where $c_{tid} \in [0, 1]$ is a coefficient weighting static disorder strength. We consider space-time uncorrelated dynamic disorder which is applied as $\Phi_{x,t} = 2\pi c_{td} \cdot \mathcal{U}[-\pi, \pi]$ for all combinations of x and t, where $c_{td} \in [0, 1]$ is a coefficient weighting dynamic disorder strength. To ensure that the QT distributions remain symmetric about the injection modes ($x = 7, 8$) as both kinds of disorder are introduced, we modulate ϕ_1 in the upper half of the array and ϕ_2 in the lower half of the array as shown in Fig. 3(a) (see Supplemental Information for details on transport symmetry).

We perform a single QT experiment by initializing the PNP to implement a symmetric QW, programming a single realization (n) of a given strength of disorder, and making a measurement of the output distribution $|\Psi_n(x, t_f)|^2$ ($t_f = 7$). Since a single realization of a level of disorder can result in a wide range of output distributions, this process is repeated over a large number of realizations (N). The

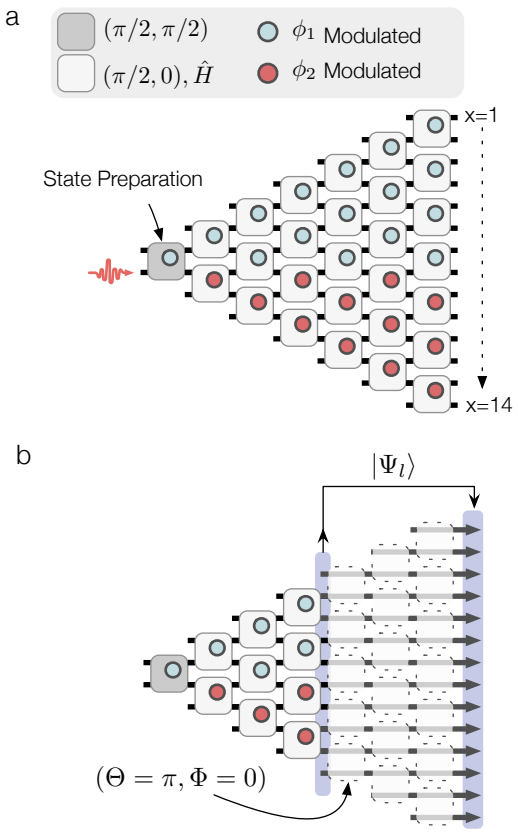

FIG. 3. **Quantum walk programs.** (a) PNP phase settings for a QW with output-mode-symmetric static and dynamic disorder response. (b) States are routed from time step 'l' to the output by programming all subsequent RBSs act as 'wires'.

ensemble average distribution is calculated as,

$$\langle |\Psi(x, t_f)|^2 \rangle = \frac{1}{N} \sum_{n=1}^{N} |\Psi_n(x, t_f)|^2 .$$

We probe temporal evolution (measurements of $\langle |\Psi(x, t)|^2 \rangle$ at each time step) by routing 'wires' $(\Theta = \pi, \Phi = 0)$ for all RBS unit cells at time steps after the time step of interest as shown in Fig. 3(b).

We will use the similarity metric[9]

$$S = \frac{\sum_{i,j} \sqrt{D_{ij} D'_{ij}}}{\sum_{i,j} D_{ij} \sum_{i,j} D'_{ij}},$$

where D_{ij} (D'_{ij}) is the experimental (computer simulated) distribution, to evaluate the closeness of our measured distribution to a computer simulated distribution.

Time-step tomography

Figure 4 shows the measured spatiotemporal evolution of the quantum walker under four distinct environmental noise

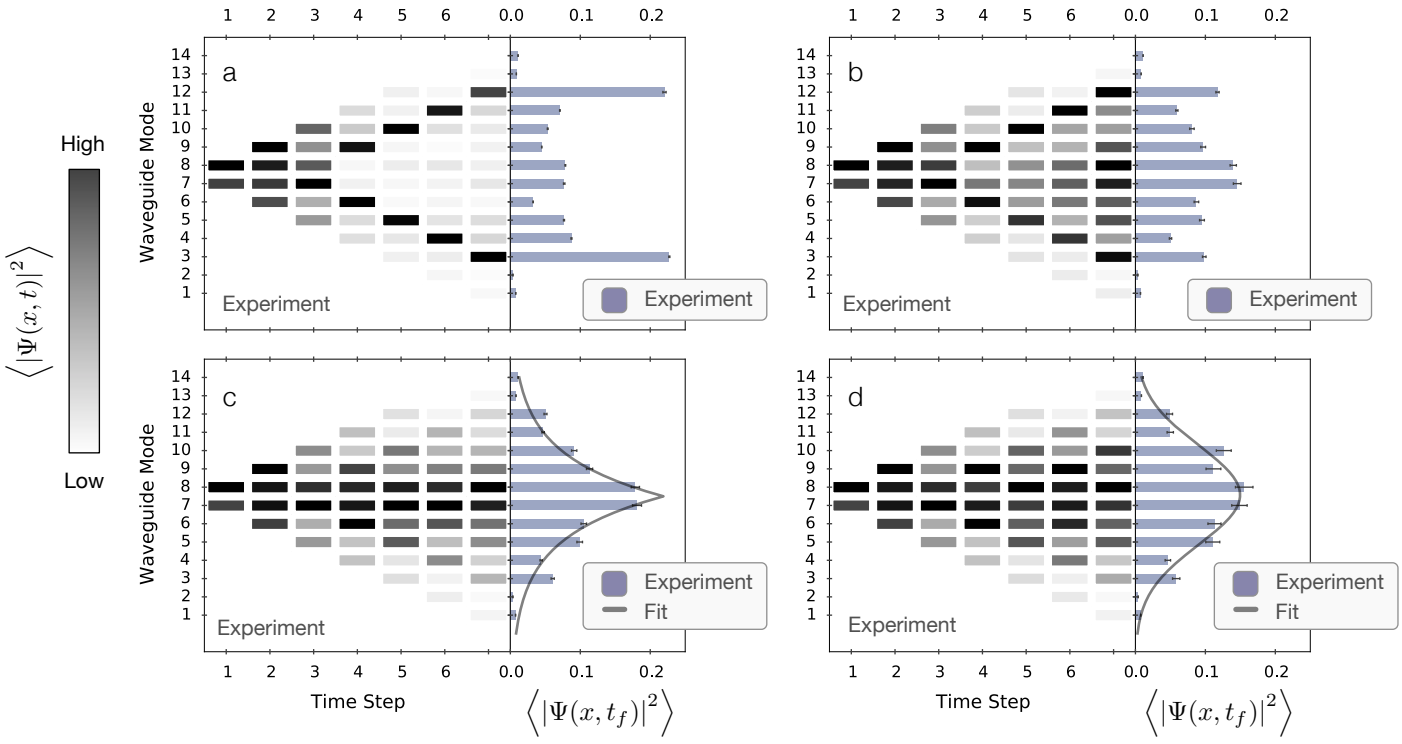

FIG. 4. **Spatiotemporal tomography.** (a-d) $\langle|\Psi(x,t)|^2\rangle\,\forall t$ (left) and $\langle|\Psi(x,t_f)|^2\rangle$ (right). (a) Ballistic transport distribution with $c_{td}=0, c_{tid}=0$. (b) Partially ballistic, partially localized distribution with $c_{td}=0, c_{tid}=0.6$. (c) Anderson localization with $c_{td}=0, c_{tid}=1$. Grey line is a Laplacian fit to the distribution. (d) Incoherent, diffusive transport with $c_{td}=1, c_{tid}=1$. Grey line is a Gaussian fit to the distribution.

conditions. We measure 200 unique unitary realizations for each level of disorder (c_{td}, c_{tid}) and time step $(t_i, 1 \leq i \leq 7)$, totaling 5,600 experiments.

First, we considered the case of an ordered QW (c_{td}, c_{tid})=(0, 0). In this case, we expect to observe a transport regime in which the distance of the quantum walker from the origin goes as $\mathcal{O}(T)$, where T is the number of time steps taken. As shown in Fig. 4(a), ballistic transport is indeed what we observe, with similarity metric values for the mean distribution of $S_t = 96.44\%$ and $S_{t_f} = 98.59\%$ for all time steps and the final time step, respectively. Next, we consider the effect of an intermediate level of static disorder (c_{td}, c_{tid})=(0, 0.6) on the output statistics. The measured distribution in Fig. 4(b) indicates intermediate levels of localization and ballistic transport characteristics $(S_t = 94.86\%, S_{t_f} = 99.40\%)$. We observe that, by adding an intermediate level of static disorder, it is possible to generate a more uniform distribution than would be possible for pure wave-like propagation or particle-like propagation. With strong static disorder (c_{td}, c_{tid})=(0, 1), the experimental data reveal an exponential localization to the initial sites (mode 7,8), as illustrated by the Laplace distribution fit in Fig. 4(c) with $S_t = 96.85\%$ and $S_{t_f} = 99.68\%$. Finally, we consider the case of a fully incoherent quantum walk with (c_{td}, c_{tid})=(1, 1). The result is shown in Fig. 4(d) with a Gaussian distribution fit which highlights the particle-like transport statistics ($S_t = 96.16\%$ and $S_{t_f} = 99.78\%$).

To discriminate between the Laplace and Gaussian distributions in Fig. 4(c,d), we computed the sum of squares residual errors as $E = \sum_i (D_i - D_i^{'})^2$ (where D is the measured distribution and $D^{'}$ is the distribution fit) for both fitting distributions. A fit of (c) with the Laplace and Gaussian distribution gives $E = 0.0028$ and $E = 0.0041$, respectively; a fit of (d) with a Gaussian and Laplace distribution gives $E = 0.0030$ and $E = 0.0057$, respectively. In both cases, the distributions we chose were a better fit for the measured data.

Environment-enhanced transport

For the next set of experiments, we measure 400 levels of disorder with $c_{td}, c_{tid} \in [0, 1]$ and 200 unique QW realizations for each level, totaling 80,000 experiments. Since the QW distributions are symmetric about the injection mode $(x = 8)$, we only need to consider modes 1-7. For modes 1, 2, 13, and 14, $\langle|\Psi(x,t_f)|^2\rangle$ is approximately constant across all disorder levels, as predicted by simulation, and so they are excluded from Fig. 5. Experimental measurements of $\langle|\Psi(x,t_f)|^2\rangle$ for modes 3-7 (illustrated in Fig. 5(a)) are shown in Fig. 5(b-f). The measured data in Fig. 5(b-f) are in excellent agreement

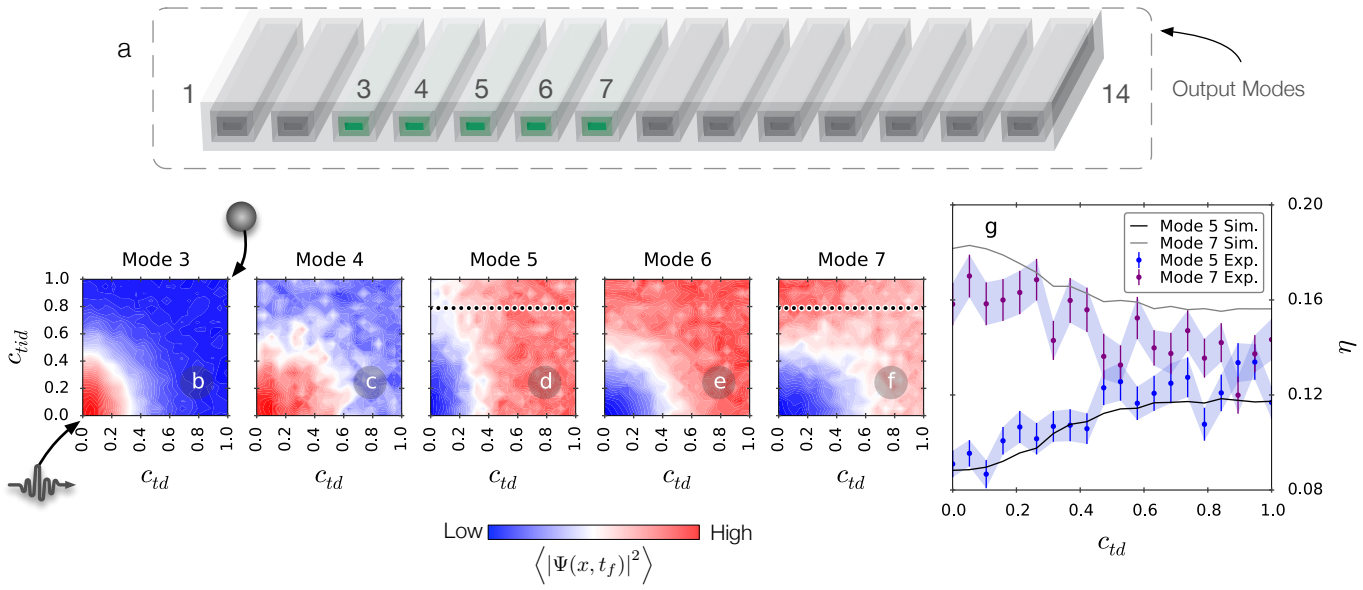

FIG. 5. **Complete transport space.** (a) Rendering of output waveguides 1-14. We plot $\langle|\Psi(x,t_f)|^2\rangle$ for modes 3, 4, 5, 6, and 7 which, due to symmetry, have the same behavior as modes 12, 11, 10, 9, and 8, respectively. We ignore modes 1, 2, 13, and 14 since they are constant across all c_{td}, c_{tid} parameters (due to the small number of possible paths that can constructively or destructively interfere on the edge of the light cone). (b-f) Experimental data corresponding to measurements of $\langle|\Psi(x,t_f)|^2\rangle$ under 400 combinations of static and dynamic disorder. Fully coherent (incoherent), wave-like (particle-like) behavior occurs in the bottom left quadrant (right edge). (g) Transport efficiency (η) through slice indicated by a dotted line along $c_{tid} = 0.842$ in (d,f). For a system with strong static disorder, the introduction of dynamic disorder enhances η for outer modes 5 and 10 while reducing transport to modes 7 and 8. Each disorder level in the computer simulation corresponds to 20,000 realizations.

with computer simulations, with final time-step similarities of $S_{t_f} = 99.77, 99.85, 99.23, 99.81, 99.83\%$ for modes 3-7, respectively.

Ballistic transport, a signature of a wave-like random walk, occurs in ordered systems. As dynamic disorder is introduced, the quantum walker decoheres, losing its wave-like character; static disorder results in localization, increasing the transport efficiency to the injection mode. As shown in the lower left quadrant of Fig. 5 (b), this is indeed the general transport behavior at mode 3. The lower left quadrant of Fig. 5(b) corresponds to ordered and nearly-ordered systems ($c_{td} \simeq 0, c_{tid} \simeq 0$) in which a quantum walker starting at mode 7 or 8 is most likely detected at mode 3 or 12. However, as disorder is introduced, the probability of detecting a quantum walker at $x = 3$ or 12 decreases. A similar behavior is observed for mode 4, as shown in Fig. 5(c).

The general behavior of modes 5, 6, and 7 shown in Fig. 1(d-f) is opposite to that of modes 3 and 4 — increased static or dynamic disorder results in increased transport efficiency to these modes with the exception of mode 5, which responds similarly for constant levels of dynamic disorder. In the regime of high static ($c_{tid} > .6$) and low dynamic ($c_{td} < 0.4$) disorder, the quantum walker is confined to modes 7 and 8 by Anderson localization, as indicated by the dark red region in the top left corner of Fig. 5(f).

Environment-assisted transport occurs in (statically) disordered systems in which transport has been arrested due to Anderson localization; through interactions with a fluctuating environment (dynamic disorder), the transport efficiency of the quantum walker may be enhanced. Rebentrost et al.[27] predicted the existence of such an effect in continuous-time QWs. However, ENAQT has not yet seen experimental or theoretical consideration for DT QWs.

Evidence of ENAQT for DT QW programs in the PNP can be found in Fig. 5(g). For strong static and weak dynamic disorder ($c_{tid} \simeq 0.8$, $c_{td} \simeq 0.$), where Anderson localization is dominant, mode 5 exhibits a striking increase in transport efficiency with the introduction of dynamic disorder. This enhancement in transport efficiency for mode 5 corresponds to a reduction in the probability for the walker to stay at origin sites ($x = 7, 8$), where the quantum walker is localized, as shown by the strong static disorder cut in Fig. 5(g). In summary, a quantum walker confined to modes 7 and 8 by Anderson localization is released through interaction with a noisy environment, increasing the quantum walker's transport efficiency to the outer modes.

To determine whether a transport optimum that is similar to the prediction for continuous-time QWs could be observed in a DT QW, we performed computer simulations of a PNP with 15 time steps. The data indicate that a transport optimum is indeed observable in systems such as the PNP (see Supplemental information for more information).

DISCUSSION

We have described the experimental observation of

environment-enhanced transport in discrete-time quantum walks over a set of 85,600 experiments spanning all combinations of static and dynamic disorder. This large number of realizations is enabled by a phase-stable, low-loss, large-scale, programmable nanophotonic processor implemented in a CMOS-compatible process. Each unit cell of the processor can implement all SU(2) rotations in the spatial-mode basis; Reck et al[30] explored a similar architecture for implementing the set of all single-particle unitary transformations (U(N)). While single-particle quantum transport simulations are easily performed with classical computers, transport simulations exceeding several tens of photons[45] become intractable[36]. Entangled photon sources[18,35] and single photon detectors[19] have recently been integrated into the silicon photonics platform, providing a path towards high photon number experiments. In addition, recently demonstrated low-latency superconducting logic devices[46] may provide fast on-chip feed-forward operations on quantum optical states. Together with programmable nanophotonic processors, these chip-integrated technologies provide a promising platform for future quantum simulation and computing tasks.

METHODS

Fabrication of the photonic circuit. We fabricated the PNP on a silicon-on-insulator wafer with 2 μm of buried SiO_2 in the Optoelectronic Systems Integration in Silicon foundry. Device regions are defined using partial- and full-etches in the silicon device layer resulting in 90 nm and 220 nm thick structures, respectively. A silica cladding 2μm thick is thermally grown on top of the device layer to achieve transverse symmetry for the optical modes. Input and output optical coupling is achieved with an inverse taper from 500 nm wide to 200 nm wide over a distance of 300μm. Light is guided in 500 nm wide by 220 nm thick silicon ridge waveguides with a single transverse-electric mode (TE0) near 1550 nm, an effective index of 2.57[43]. Thermo-optic phase shifters[35] are defined by full- and partial-etches and two Boron implants with concentrations $7{\cdot}10^{17}$ cm^{-3} and $1.7{\cdot}10^{20}$ cm^{-3}. We chose an electronic 'acceptor' dopant over a 'donor' dopant since the free-carrier absorption is less for free holes than free electrons[47]. Due to high active element densities, two aluminum layers and two via layers are required to simplify the phase shifter electrical signal routing.

ACKNOWLEDGMENTS

This work was supported in part by the Air Force Office of Scientific Research Multidisciplinary University Research Initiative (FA9550-14-1-0052) and the Air Force Research Laboratory RITA program (FA8750-14-2-0120). M.H. acknowledges support from AFOSR STTR grants, numbers FA9550-12-C-0079 and FA9550-12-C-0038 and Gernot Pomrenke, of AFOSR, for his support of the OpSIS effort, though both a PECASE award (FA9550-13-1-0027) and funding for OpSIS (FA9550-10-1-0439). N. H. acknowledges support from the National Science Foundation Graduate Research Fellowship grant no. 1122374. G.S. acknowledges support from the Department of Defense National Science and Engineering Graduate Fellowship. D.E. acknowledges support from the Sloan Research Fellowship in Physics. Y.L. acknowledges support from the Pappalardo Fellowship in Physics. The authors thank Christophe Galland for his helpful discussions of the result.

AUTHOR CONTRIBUTIONS

N.H. designed the system with assistance from J.M. and D.E.. G.S., N.H., and J.M. designed and implemented the experimental apparatus. G.S., N.H., and M.P. calibrated the system. N.H., Y.L., S.L. and D.E. conceived the quantum transport experiment. T.B.J. and M.H. fabricated the system. N.H., D.E., Y.L., and G.S. wrote the paper.

REFERENCES

[1] Schmitz, H. *et al.* Quantum walk of a trapped ion in phase space. *Physical Review Letters* **103** (2009). URL http://dx.doi.org/10.1103/PhysRevLett.103.090504.

[2] Zahringer, F. *et al.* Realization of a quantum walk with one and two trapped ions. *Physical Review Letters* **104** (2010). URL http://dx.doi.org/10.1103/PhysRevLett.104.100503.

[3] Preiss, P. M. *et al.* Strongly correlated quantum walks in optical lattices. *Science* **347** (2015). URL http://dx.doi.org/10.1126/science.1260364.

[4] Broome, M. A. *et al.* Discrete single-photon quantum walks with tunable decoherence. *Physical Review Letters* **104** (2010). URL http://dx.doi.org/10.1103/PhysRevLett.104.153602.

[5] SvozilÃŋk, J., LeÃșn-Montiel, R. d. J. & Torres, J. P. Implementation of a spatial two-dimensional quantum random walk with tunable decoherence. *Phys. Rev. A* **86** (2012). URL http://dx.doi.org/10.1103/PhysRevA.86.052327.

[6] Kitagawa, T. *et al.* Observation of topologically protected bound states in photonic quantum walks. *Nature Communications* **3** (2012). URL http://dx.doi.org/10.1038/ncomms1872.

[7] Jeong, Y.-C., Di Franco, C., Lim, H.-T., Kim, M. & Kim, Y.-H. Experimental realization of a delayed-choice quantum walk. *Nature Communications* **4** (2013). URL http://dx.doi.org/10.1038/ncomms3471.

[8] Schreiber, A. *et al.* Photons walking the line: A quantum walk with adjustable coin operations. *Physical Review Letters* **104** (2010). URL http://dx.doi.org/10.1103/PhysRevLett.104.050502.

[9] Crespi, A. *et al.* Anderson localization of entangled photons in an integrated quantum walk. *Nature Photon* **7** (2013). URL http://dx.doi.org/10.1038/nphoton.2013.26.

[10] Schwartz, T., Bartal, G., Fishman, S. & Segev, M. Transport and anderson localization in disordered two-dimensional photonic lattices. *Nature* **446** (2007). URL http://dx.doi.org/10.1038/nature05623.

[11] Lahini, Y. *et al.* Anderson localization and nonlinearity in one-dimensional disordered photonic lattices. *Physical Review Letters* **100** (2008). URL http://dx.doi.org/10.1103/PhysRevLett.100.013906.

[12] Schreiber, A. *et al.* Decoherence and disorder in quantum walks: From ballistic spread to localization. *Physical Review Letters* **106** (2011). URL http://dx.doi.org/10.1103/PhysRevLett.106.180403.

[13] Bromberg, Y., Lahini, Y., Morandotti, R. & Silberberg, Y. Quantum and classical correlations in waveguide lattices. *Physical Review Let-*

ters **102** (2009). URL http://dx.doi.org/10.1103/PhysRevLett.102.253904.

[14]Peruzzo, A. *et al.* Quantum walks of correlated photons. *Science* **329** (2010). URL http://dx.doi.org/10.1126/science.1193515.

[15]Sansoni, L. *et al.* Two-particle bosonic-fermionic quantum walk via integrated photonics. *Physical Review Letters* **108** (2012). URL http://dx.doi.org/10.1103/PhysRevLett.108.010502.

[16]Perets, H. B. *et al.* Realization of quantum walks with negligible decoherence in waveguide lattices. *Physical Review Letters* **100** (2008). URL http://dx.doi.org/10.1103/PhysRevLett.100.170506.

[17]Harris, N. C. *et al.* Integrated source of spectrally filtered correlated photons for large-scale quantum photonic systems. *Physical Review X* **4** (2014). URL http://dx.doi.org/10.1103/PhysRevX.4.041047.

[18]Collins, M. *et al.* Integrated spatial multiplexing of heralded single-photon sources. *Nature Communications* **4** (2013). URL http://dx.doi.org/10.1038/ncomms3582.

[19]Najafi, F. *et al.* On-chip detection of non-classical light by scalable integration of single-photon detectors. *Nature Communications* **6** (2015). URL http://dx.doi.org/10.1038/ncomms6873.

[20]Aspuru-Guzik, A. & Walther, P. Photonic quantum simulators. *Nat Phys* **8** (2012). URL http://dx.doi.org/10.1038/nphys2253.

[21]Huh, J., Guerreschi, G. G., Peropadre, B., McClean, J. R. & Aspuru-Guzik, A. Boson sampling for molecular vibronic spectra. *arXiv preprint arXiv:1412.8427* (2014).

[22]Levi, L., Krivolapov, Y., Fishman, S. & Segev, M. Hyper-transport of light and stochastic acceleration by evolving disorder. *Nat Phys* **8** (2012). URL http://dx.doi.org/10.1038/nphys2463.

[23]Amir, A., Lahini, Y. & Perets, H. B. Classical diffusion of a quantum particle in a noisy environment. *Phys. Rev. E* **79** (2009). URL http://dx.doi.org/10.1103/PhysRevE.79.050105.

[24]Anderson, P. W. Absence of diffusion in certain random lattices. *Phys. Rev.* **109** (1958). URL http://dx.doi.org/10.1103/PhysRev.109.1492.

[25]Lahini, Y., Bromberg, Y., Christodoulides, D. N. & Silberberg, Y. Quantum correlations in two-particle anderson localization. *Physical Review Letters* **105** (2010). URL http://dx.doi.org/10.1103/PhysRevLett.105.163905.

[26]Segev, M., Silberberg, Y. & Christodoulides, D. N. Anderson localization of light. *Nature Photon* **7** (2013). URL http://dx.doi.org/10.1038/nphoton.2013.30.

[27]Rebentrost, P., Mohseni, M., Kassal, I., Lloyd, S. & Aspuru-Guzik, A. Environment-assisted quantum transport. *New Journal of Physics* **11** (2009). URL http://dx.doi.org/10.1088/1367-2630/11/3/033003.

[28]Mohseni, M., Rebentrost, P., Lloyd, S. & Aspuru-Guzik, A. Environment-assisted quantum walks in photosynthetic energy transfer. *The Journal of Chemical Physics* **129** (2008). URL http://dx.doi.org/10.1063/1.3002335.

[29]Caruso, F., Spagnolo, N., Vitelli, C., Sciarrino, F. & Plenio, M. B. Simulation of noise-assisted transport via optical cavity networks. *Phys. Rev. A* **83** (2011). URL http://dx.doi.org/10.1103/PhysRevA.83.013811.

[30]Reck, M. & Zeilinger, A. Experimental realization of any discrete unitary operator. *Physical Review Letters* **73** (1994). URL http://dx.doi.org/10.1103/PhysRevLett.73.58.

[31]Miller, D. A. B. Self-configuring universal linear optical component [invited]. *Photonics Research* **1** (2013). URL http://dx.doi.org/10.1364/PRJ.1.000001.

[32]Mower, J., Harris, N. C., Steinbrecher, G. R., Lahini, Y. & Englund, D. High-fidelity quantum photonics on a programmable integrated circuit. *arXiv preprint arXiv:1406.3255* (2014).

[33]Carolan, J. *et al.* Universal linear optics. *arXiv preprint arXiv:1505.01182* (2015).

[34]Biberman, A., Timurdogan, E., Zortman, W. A., Trotter, D. C. & Watts, M. R. Adiabatic microring modulators. *Optics Express* **20** (2012). URL http://dx.doi.org/10.1364/OE.20.029223.

[35]Harris, N. C. *et al.* Efficient, compact and low loss thermo-optic phase shifter in silicon. *Optics Express* **22** (2014). URL http://dx.doi.org/10.1364/OE.22.010487.

[36]Aaronson, S. & Arkhipov, A. The computational complexity of linear optics. *Proceedings of the 43rd annual ACM symposium on Theory of computing - STOC 2011* (2011). URL http://dx.doi.org/10.1145/1993636.1993682.

[37]Spring, J. B. *et al.* Boson sampling on a photonic chip. *Science* **339** (2012). URL http://dx.doi.org/10.1126/science.1231692.

[38]Broome, M. A. *et al.* Photonic boson sampling in a tunable circuit. *Science* **339** (2012). URL http://dx.doi.org/10.1126/science.1231440.

[39]Prevedel, R. *et al.* High-speed linear optics quantum computing using active feed-forward. *Nature* **445** (2007). URL http://dx.doi.org/10.1038/nature05346.

[40]Knill, E., Laflamme, R. & Milburn, G. J. *Nature* **409** (2001). URL http://dx.doi.org/10.1038/35051009.

[41]Kok, P. *et al.* Linear optical quantum computing with photonic qubits. *Rev. Mod. Phys.* **79** (2007). URL http://dx.doi.org/10.1103/RevModPhys.79.135.

[42]Childs, A. M. Universal computation by quantum walk. *Phys. Rev. Lett.* **102**, 180501 (2009). URL http://link.aps.org/doi/10.1103/PhysRevLett.102.180501.

[43]Baehr-Jones, T. *et al.* A 25 Gb/s Silicon Photonics Platform. *ArXiv e-prints* (2012). URL http://adsabs.harvard.edu/abs/2012arXiv1203.0767B. 1203.0767.

[44]Yang, Y. *et al.* Phase coherence length in silicon photonic platform. *Optics Express* **23** (2015). URL http://dx.doi.org/10.1364/OE.23.016890.

[45]Yao, X.-C. *et al.* Observation of eight-photon entanglement. *Nature Photon* **6** (2012). URL http://dx.doi.org/10.1038/nphoton.2011.354.

[46]McCaughan, A. N. & Berggren, K. K. A superconducting-nanowire three-terminal electrothermal device. *Nano Lett.* **14** (2014). URL http://dx.doi.org/10.1021/nl502629x.

[47]Soref, R. & Bennett, B. Electrooptical effects in silicon. *IEEE Journal of Quantum Electronics* **23** (1987). URL http://dx.doi.org/10.1109/JQE.1987.1073206.